
Article:
Fukagai, S., Marshall, M. and Lewis, R. (2022) Transition of the friction behaviour and contact stiffness due to repeated high-pressure contact and slip. Tribology International, 170. 107487. ISSN: 0301-679X

https://doi.org/10.1016/j.triboint.2022.107487

Transition of the friction behaviour and contact stiffness due to repeated high-pressure contact and slip

S. Fukagai[a,b,*], M.B. Marshall[b], R. Lewis[b]

[a] Railway Technical Research Institute, Tokyo, Japan

[b] Department of Mechanical Engineering, University of Sheffield, Sheffield, UK

* corresponding author: fukagai.shinya.81@rtri.or.jp

Abstract

A rapid increase in the friction coefficient can occur during the running-in between the wheel and rail. Although it has been found that the running-in process depends on the initial topography, the difficulty in obtaining accurate non-destructive interfacial measurements has hindered systematic investigations. In this work, four interfaces, which have different initial topographies, were continuously monitored using ultrasound reflectometry until they became conformal. A contact pressure representative of that in a wheel-rail interface was achieved by using a high-pressure torsion test approach. The transition of contact stiffness and friction coefficient with repeated slip and their relationship were investigated. Based on the experimental results, a mechanistic model for the running-in process of the contact interface was proposed. These findings will help in understanding the running-in process of the wheel-rail interface and assist in managing the wheel and rail appropriately to improve safety. A common insight into the running-in process for metal-to-metal contacts under high contact pressures has also been developed.

1. Introduction

The wheel and the rail play vital roles in rail operation, such as bearing the vehicle load, guiding the vehicle and transmitting the driving and braking forces. To achieve these roles, the wheel and the rail roll and slide against each other under extremely high contact pressure conditions. Due to the severe contact condition, the interface is the origin of a number of tribological problems during operation. For example, when contaminants, such as water, oil or fallen leaves, get into the interface wheel spin and brake lock-up can sometimes occur. Such significant sliding can cause not only performance problems in terms of delays and safety issues from over-running (past signals at danger or a station), but also thermal damage and abnormal deformation of wheels and rails [1,2]. When travelling in a curve, the contact position of the inner and outer wheels is different, but because of the tapered profile of the wheel, the diameter of the wheel at the contact point with the rail is different between them [3]. In other words, the outer wheel diameter is larger than the inner wheel diameter to allow smooth passage of a train. On sharp curves, however, such a difference in wheel diameter is

insufficient and a large slip occurs in the contact area. Here, it is known that the friction force with slip at sharp curves could lead to severe wear and deformation of wheels and rails [4,5], high energy consumption [6] and wheel-rail noise [7,8]. Additionally, it increases the risk of a wheel climb derailment occurring [9–11].

One parameter that has a significant impact on these problems is the friction coefficient. The friction coefficient is a system-dependent value, and it is generally known that the value depends on various environmental conditions, e.g., temperature, humidity, contamination, etc. Surface topography is also an influencing factors. For example, it has been reported that wheels with lathe cutting marks just after wheel re-profiling are prone to derailment [12–14]. However, the effect of such topography is still not well understood. The authors have already investigated the influence of the topography on the friction behaviour between the wheel and rail in dry condition focusing on the mechanism of the flange climb-up derailment [15]. Figure 1 shows the schematic change of the traction coefficient in the climbing direction with time, obtained from a twin-disc test. The surfaces of the rail disc and wheel disc-A were finished with grinding, while the surfaces of the wheel disc-B and disc-C were deliberately left with machining marks of different cutting pitches to simulate a re-profiled wheel. As a result, it was found that the initial topography strongly affected the friction behaviour during running-in. Stage-I is the state before the test, Stage-II is the state near the peak traction coefficient and Stage-III is the state after the running-in. The rougher the initial surface profile is, the longer it takes to reach the peak value. This seemed to indicate that the surface roughness was plastically deformed until the surface conformation was completed and that wear started after the friction coefficient had reached its peak. Similar behaviour has been reported not only in twin-disc tests, but also in reciprocating sliding experiments [16,17]. These results suggest that friction coefficient changes dramatically with surface conditions such as geometry during the running-in process in dry conditions, and that these changes are strongly influenced by the initial geometry.However these findings were based on surface investigations when the test was stopped intermittently. To further improve understanding of how evolution of roughness affects friction non-destructive interfacial measurements are required. The lack of suitable techniques for facilitating this has hindered systematic investigations.

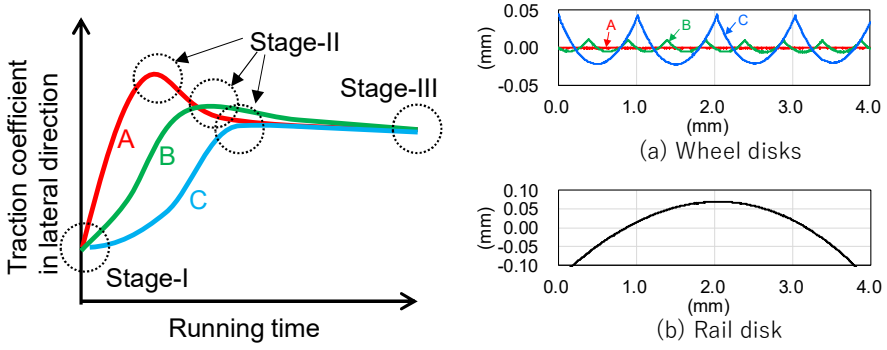

Fig. 1 Schematic patterns of the traction coefficient curves at the twin-disc tests during running-in [15]; the initial roughness is greater in the order of C, B, and A. The rougher the initial surface profile is, the longer it takes to reach the peak value.

Recently, ultrasound techniques have been used to observe the contact between wheel and rail [18–25]. Although there are spatial resolution limits and considerations of transducer positioning to ensure the sound waves reflect off the area of interest, this technique can be used to non-invasively and directly observe the contact. When an ultrasound wave strikes the interface between the wheel and rail, it is partially transmitted and partially reflected. The proportion of the wave reflected depends on the stiffness of the contact [26,27]. This approach has been used to determine the contact pressure distribution in wheel-rail contacts and the influence of wear profile, roughness and surface defects on the contact patch [19,21]. This actual distribution of the contact pressure could be applied to the simulation of wear and damage propagation with consideration for surface topography [28,29]. Additionally, a fundamental study to investigate theinterfacial condition with micro-periodic vibration using ultrasonic waves was reported [30,31].

The authors applied the ultrasound reflectometry to an actual wheel-rail interface and monitored the changes in the interface condition during repeated rolling [32,33]. The results showed that there was a correlation between the change in friction coefficient and contact stiffness with repeated rolling-sliding, and a near linear relationship was obtained. Additionally, the authors also applied the ultrasonic measurement technique to the high-pressure torsion (HPT) test and investigated the dynamic change of contact stiffness with slip [34]. As a result, it was found that the deformation of surface asperities and frictional behaviour due to slip differed depending on the surface topography. The above report is limited to the measurement of friction during one test cycle, but if an interface where sliding cycles are repeated can be continuously monitored, the mechanism of the continuously changing friction coefficient during the running-in as shown in Fig. 1 may be revealed.

The aim of this work was to investigate what is happening at the wheel-rail interface during the running-in process and how the behaviour influences evolution of friction. To achieve a contact pressure equivalent to the wheel-rail contact, a high-pressure torsion test approach was used. Tiny piezoelectric elements which activate the ultrasound wave were attached to the one of the specimens. Ultrasonic reflection from the interface was used to conduct an in-situ evaluation of the contact condition, particularly contact stiffness. Transient loading condition and friction coefficient were also measured during the test. Following these measurements, the changes of contact stiffness with repetitive slip cycles and the running-in mechanism were proposed.

2. Methodology

2.1 HPT testing equipment

Since the details of the high-pressure torsion test equipment and ultrasonic measurement are described in previous works [34,35] only the basic structure is explained here. Figure 2 shows the appearance of the HPT testing equipment. This is capable of making contact between two specimens with a constant normal pressure and then rotating the bottom specimen in the direction parallel to the contact interface. It uses load cells for tension, compression, and torque to measure the compressing load and the torque; and uses a rotary variable differential transformer to measure the rotation speed. Table 1 lists the specifications of the HPT testing equipment.

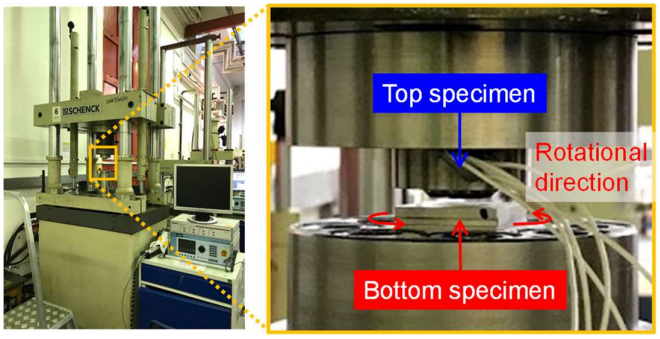

Fig.2 Appearance of the HPT equipment

Table 1 Specifications of the HPT testing equipment

Item	Value
Axial load (tensile and compression)	±400 kN
Movable range in axial direction	±25 mm
Torque	±1000 Nm
Movable range in rotational direction	±40 degrees

2.2 Ultrasonic measurement

In this study, the contact stiffness was measured in three directions: normal and two tangential directions, slip direction and perpendicular to the slip direction, based on the intensity of the ultrasonic wave reflected from the contact interface. In the following, the principle of the evaluation of contact phenomena by ultrasonic reflectometry will be explained.

Since the details of the ultrasonic measurement of an interface are described in many previous studies [19,23,32,35–37], only the basic principles are explained here. At the interface between materials with different acoustic impedances, only a part of a sound wave transmits at the interface and the rest of it is reflected back. The reflectivity for ultrasound at an interface where the materials

adhere to each other without any cavities, R, can be represented as in Equation (1) and it varies depending on the difference in the acoustic impedances of the two materials.

$$R = \frac{z_2 - z_1}{z_2 + z_1} \quad (1)$$

In this equation, z_1 and z_2 are the acoustic impedances of the materials in contact. The acoustic impedance is determined by the product of the density of the material and the acoustic velocity in the material. Therefore, when the acoustic impedances of the two materials in contact are the same and if the interface is hypothetically perfectly conformal, all the sound wave will transmit at the interface without any loss and no reflection occurs (R=0). On the other hand, when materials with significantly different acoustic impedances, such as a gas and a solid, are in contact, sound waves are almost completely reflected (R≈1).

Figure 3 shows a schematic model of an ideal asperity contact loaded in both the normal and tangential directions. The surface of an actual material is not perfectly flat, but has micro-asperities and undulations, so that when two bodies come into contact, an interface with air cavities is created. When the wavelength of the ultrasound is sufficiently larger than the cavity size at the interface, the proportion of the reflected wave also depends on the contact stiffness. The contact stiffness is a function of the number, size, and approach of the contact points determined while considering the minute asperities [26]. Because the topographies of the surface changes due to elastic and plastic deformation, the measured reflectivity changes as shown in Fig. 3 as load is applied. Therefore, it is possible to evaluate the contact stiffness at the interface by using the reflectivity of ultrasound. Generally, the contact stiffness is defined as the normal or tangential stress generated when the relative distance between two surfaces in contact via surface asperities changes by a unit length in each direction.

The contact stiffnesses for each direction are expressed as shown in the following equations:

$$K_N = \frac{d\sigma_N}{d\delta_N} \quad , \quad (2)$$

$$K_T = \frac{d\sigma_T}{d\delta_T} \quad , \quad (3)$$

where σ_N and σ_T are the normal and tangential stresses, respectively. It is often interpreted that δ_N is the approaching distance between the average height of the roughness asperities distributed on the two contacting surfaces, and δ_T is the relative distance in the tangential direction between the asperities on the two contacting surfaces (Fig. 3) [38–42].

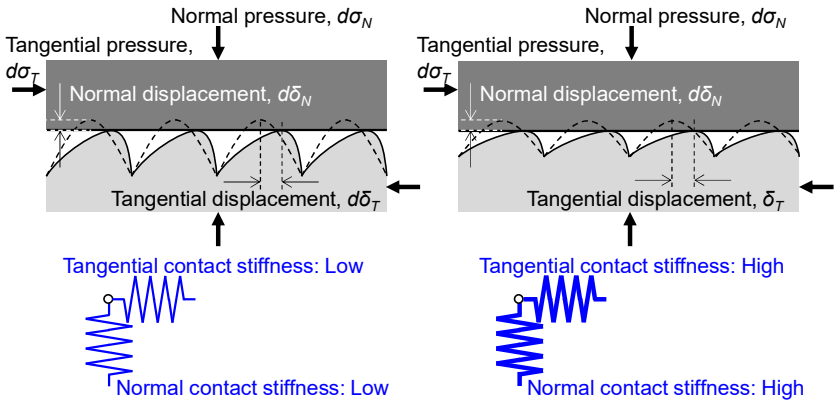

Fig. 3 Schematic model of an imperfect interface with ideal asperities. Normal and tangential loads are simulated.

2.3 Specimens

The top and the bottom specimens were made from ER8 (EN13262:2009) and R260 (EN13674-1:2011), respectively. Table 2 shows the hardness for the specimens. The hardness values are the average for 5 measurements. The measurements were conducted by a Mitutoyo HV-110 machine and test force was 5 kgf.

Table 2 Hardness of the specimens

	R8T Wheel (top) specimen	R260 Rail (bottom) specimen
Hardness HV(5)	267	285

The surface type of the top specimens remained constant for all tests and was achieved by grinding. On the other hand, the surface types of bottom specimens were varied. Four different roughness' were used: a low roughness specimen achieved by sand blasting and medium and large roughness specimens achieved by machining (fly cut), which gave increasingly high values. Figure 4 shows the appearance of specimens on the contact surface.

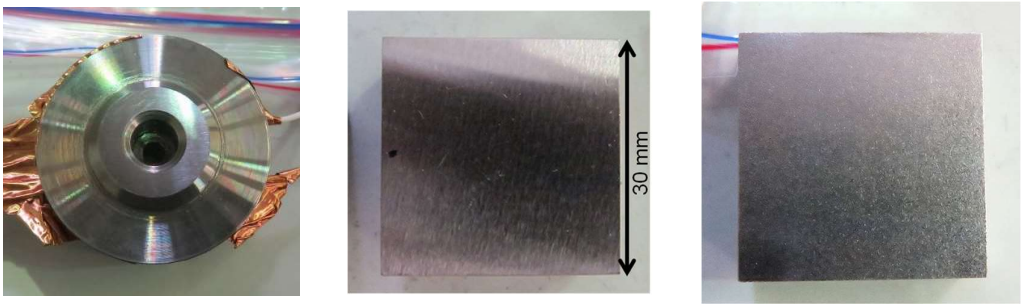

(a) Top specimen (b) Bottom specimen: (c) Bottom specimen:

Low roughness

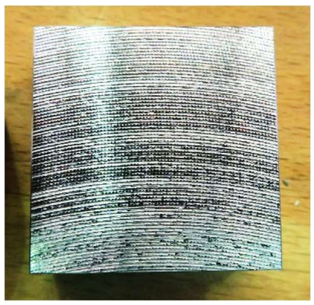

(d) Bottom specimen: High roughness (Cutting pitch: 0.4 mm)

Medium roughness

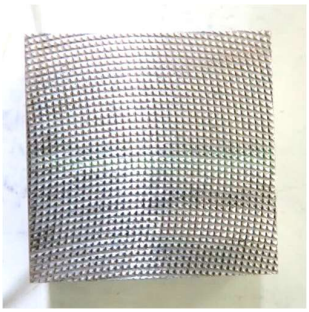

(e) Bottom specimen: High roughness (Cutting pitch: 0.8 mm)

Fig. 4 Appearance of specimens on the contact side.

Table 3 lists the values of the root-mean-square of roughness which were measured using a contact-type roughness meter (Mitsutoyo Surf Test SJ-210) with a cut-off of 0.8 mm and a length of 2.4 mm. The value of the root-mean-square of roughness is the average value for 5 measurements.

The value of the combined roughness, σ, is calculated using equation (4);

$$\sigma = \sqrt{{R_{qt}}^2 + {R_{qb}}^2} \tag{4}$$

where R_{qt} and R_{qb} are the root mean square roughness of the top and bottom specimens, respectively.

Table 3 Roughness' of specimen's surface before the tests for topography dependence.

Topography	Normal pressure (MPa)	Measurement direction	Root-mean-square of roughness, Rq (μm)		Combined roughness for each direction (μm)
			Top specimen	Bottom specimen	
Low roughness	600	Circumferential	0.5	0.7	0.8
		Radial	0.6	0.6	0.9
Medium roughness	600	Circumferential	0.3	1.4	1.5
		Radial	0.4	1.5	1.6
High roughness (0.4 mm)	600	Circumferential	0.6	5.7	5.8
		Radial	0.8	2.7	2.8
High roughness	600	Circumferential	0.6	7.4	7.4

(0.8 mm)		Radial	0.7	8.0	8.1
	300	Circumferential	2.3	7.3	7.7
		Radial	2.3	8.9	9.2
	900	Circumferential	0.3	10.2	10.2
		Radial	0.3	9.7	9.7

For all the contact tests, specimens were soaked in 2-propanol before the measurement and then washed in an ultrasonic bath. Piezoelectric elements were attached to the top specimen to reflect the ultrasound towards the contact interface and measure the reflected wave. Figure 5 shows the piezoelectric element which was attached on the back of the top specimen. The piezoelectric elements were attached to respectively measure the longitudinal and transverse waves to determine the contact stiffness in the normal, tangential direction, because there is a possibility the contact stiffness' in different directions show varying characteristic behaviour with application of the normal and tangential pressure. The piezoelectric elements for measurement of the transverse waves were installed in directions parallel (circumferential direction) and perpendicular (radial direction) to the friction direction. Piezoelectric elements with a central frequency of 5 MHz were used for both the measurements of longitudinal and transverse waves.

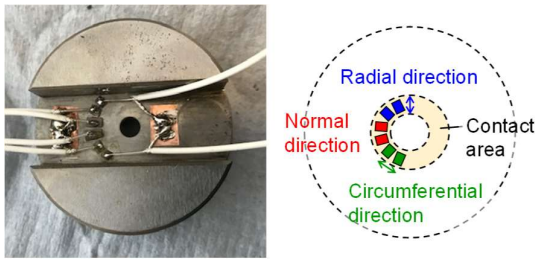

Fig. 5 Piezoelectric element which is attached on the back of the top specimen

The longitudinal element oscillates a wave in which the displacement of the medium coincides with the direction of motion of the wave, while the transverse element oscillates a wave in which the displacement of the medium is perpendicular to the direction of motion of the wave. The longitudinal and transverse waves reflected on the interface contain information about the contact stiffness in the normal and tangential directions, respectively.

When the frictional force acts on the interface, the tangential contact stiffness may behave differently from normal contact stiffness. In particular, the contact stiffness in the tangential direction may also be different between the perpendicular (radial) direction and the slip (circumferential) direction.

2.4 Test procedure

Figure 6 shows a schematic of the experimental set-up. A 20V peak-to-peak, 5MHz, 3-cycle, sine wave was generated by a function generator (TG5011A, AIM-TTI Instruments) and used to excite the piezoelectric elements on the actuator side and generate an ultrasonic wave. The ultrasonic waves then propagated to the contact interface, and the wave reflected from the interface was received by the piezoelectric elements on the sensor side. The received waveforms were digitized without any amplification using a digital oscilloscope (Picoscope 5000 series, PicoTech), and stored on a PC. The information from the HPT controller (normal load, torque and rotation position) was obtained off-line, but a part of the information (normal load) was shared by the oscilloscope and used to synchronize the ultrasonic and HPT data in post-processing.

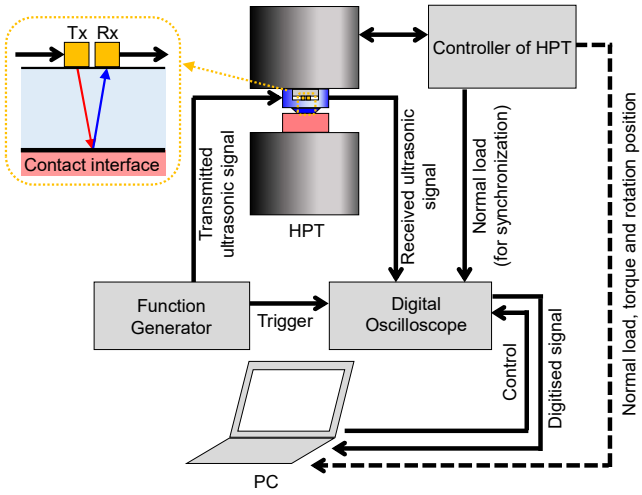

Fig. 6 Schematic of whole experiment setup.

The measured reflection waveforms were bandpass filtered from 3 MHz to 7 MHz. Figure 7 shows examples of reflected waveforms of a longitudinal wave after band-pass filtering. Two cases are shown here, with and without contact. The values between the maximum and minimum peaks were used as the evaluation values in the time domain.

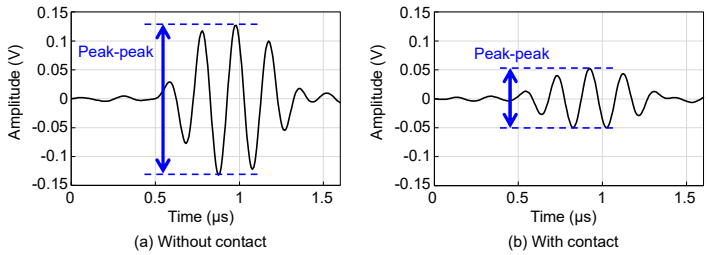

Fig. 7 Examples of reflected waveforms of longitudinal wave after band-pass filter.

A test was conducted using the following procedure:

1. A normal pressure is applied after inserting a pressure-sensitive paper between the specimens to check that the load is uniformly distributed on the contact surface.
2. After making the specimens directly contact with each other, the pressure on the contact surface is increased gradually to approximately 600MPa (Additionally, 300 MPa in the case of high roughness).
3. While keeping the top specimen in the specified position, the bottom specimen is rotated.
4. After releasing the torque, the specimens are separated.
5. Back to step 2.

During steps 2 to 4, the contact stiffness is measured by using ultrasound with normal force (normal pressure), torque (tangential pressure), and the rotational position of the specimen (Fig. 8). Steps 2 to 5 were repeated until 15 cycles and the roughnesses of top and bottom specimens were measured after 1st, 5^{th}, 10^{th} and 15^{th} cycle. The roughnesses were measured five times for each of the radial and circumferential directions of the specimen rotation and the average value was evaluated.

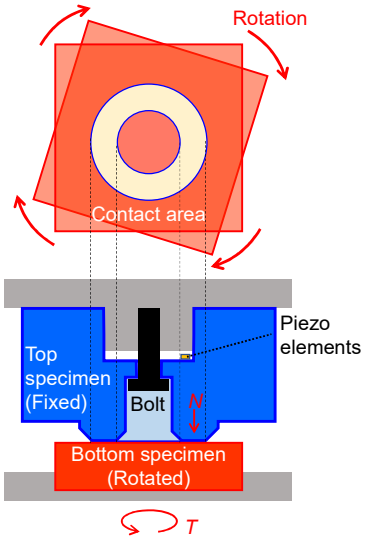

Fig. 8 Contact between top and bottom specimens and rotation of bottom specimen.

Figure 9 shows a schematic example of a change of contact pressure and sample rotation position between test steps 2-4. Normal force (normal pressure), torque (tangential pressure) and contact stiffness for each test cycle were evaluated by calculating the average value for a given time. In order to eliminate making an arbitrary evaluation, the time interval was standardized as 3 seconds before the signal to start the release of torque was sent, and the average value during that time was obtained.

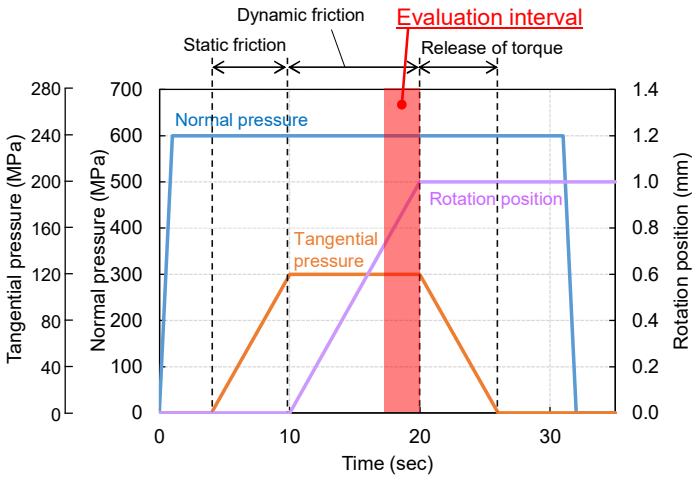

Fig. 9 Schematic example of a loading cycle

3. Results

3.1 Topography dependence on contact stiffness and friction coefficient during running-in

Figure 10 shows the change of friction coefficient with test cycles for different initial roughness. It is found that the lower the initial roughness, the faster the friction coefficient rises, and the peak friction coefficient is higher for lower initial roughness. It can also be seen that the friction coefficient reaches around 0.6 in the final state of the 15th cycle for all roughness conditions. These tendencies of change coincide well with the patterns which were obtained from the results using a twin-disc machine (Figure 1).

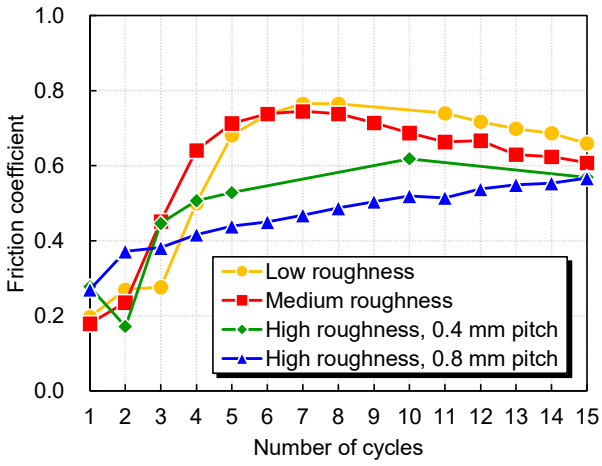

Fig. 10 Change of friction coefficient with test cycles for different initial roughness.

Figure 11 shows the changes of contact stiffness and friction coefficient with testing cycles for different initial roughness. It is found that the stiffness in the cases of low and medium roughness peaked in the early cycles, 4th-5th, then dropped until the 8th-10th test cycle, then tapered off until the 15th test cycle. In the case of high roughness, 0.4 mm pitch, the contact stiffness rose gradually until the 5th or 10th cycle, then kept constant or tapered until the 15th test cycle. In the case of high roughness, 0.8 mm pitch, the stiffness gradually increased through all the test cycles. A generally good correlation was obtained between the contact stiffness and the friction coefficient. The friction coefficient was at its maximum at about the same time as the contact stiffness was at its maximum.

By comparing the changes in all roughness conditions, it was observed that the lower the initial roughness, the faster the increase in contact stiffness and the higher the peak contact stiffness for all cycles. For all roughness conditions, normal stiffness was higher than the shear stiffnesses after the 6th cycle. This is in agreement with previous studies such as Gonzalez-Vadez *et al*. [39]. Furthermore, in this experiment, the shear stiffness in the circumferential direction tended to be higher than that in the radial direction for most of the test cycles, especially for smoother surfaces. These direction-dependent properties were not clear in the previously reported single-cycle results[34]. Figures 11(b) and 11(d) show that this tendency appears in the later cycles.

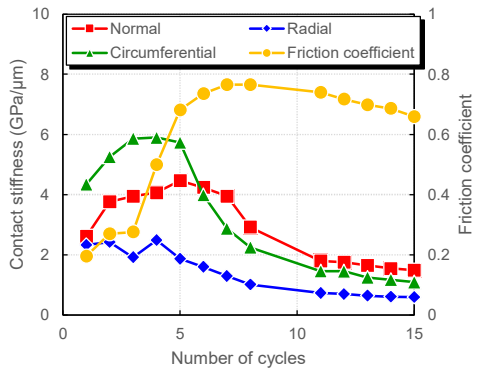

(a) Low roughness

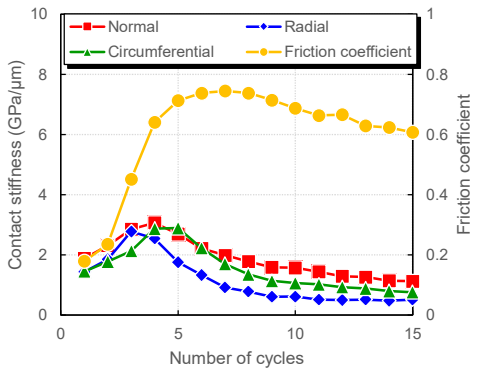

(b) Medium roughness

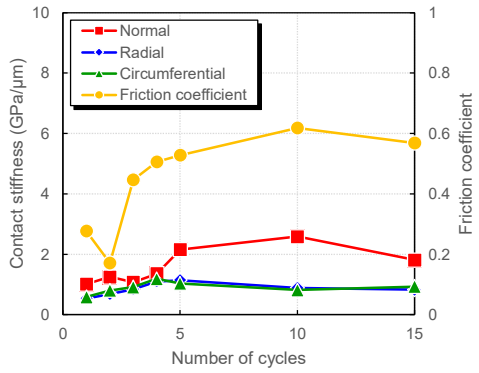

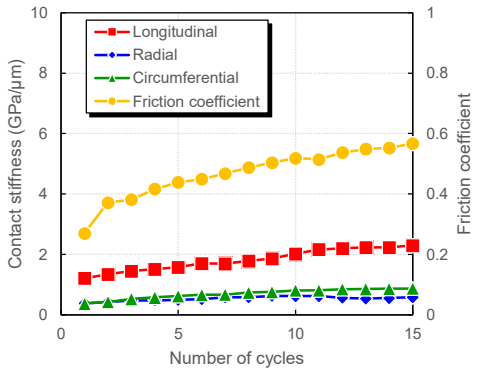

(c) High roughness, 0.4 mm pitch (d) High roughness, 0.8 mm pitch

Fig. 11 Changes of contact stiffness and friction coefficient with test cycles for different initial roughness.

Figure 12 shows the relationship between normal contact stiffness and friction coefficient during cycles. Although there is a generally positive correlation between the friction coefficient and the contact stiffness, the correlation appears to be dependent on the initial topography conditions. The higher the initial roughness, the more linear the relationship between contact stiffness and friction coefficient, and the lower the initial roughness, the more gradual the relationship between the contact stiffness and the friction coefficient at the beginning of cycles. In other words, at the beginning of the cycle with low roughness, a small tangential (friction) force caused a large increase in contact stiffness.

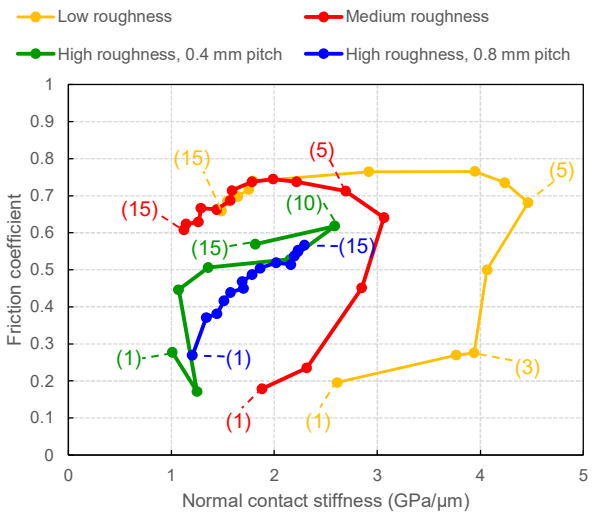

Fig. 12 Relationship between normal contact stiffness and friction coefficient during cycles. Number in brackets is the cycles.

3.2 Contact pressure dependence on contact stiffness and friction coefficient during running-in

Figure 13 shows the change of friction coefficient with test cycles for different contact pressures under high roughness conditions (0.8 mm pitch). In the case of 600 and 900 MPa, there was a reversal of the high and low values when the number of cycles was low, but basically, the friction coefficient in the running-in process increased with the increase in contact pressure.

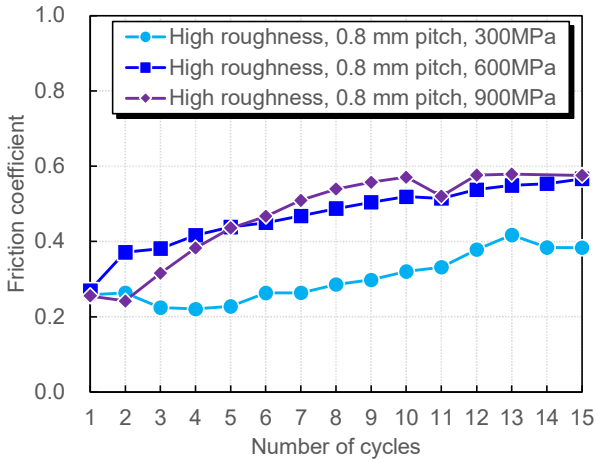

Fig. 13 Change of friction coefficient with test cycles for different contact pressure under high roughness conditions (0.8 mm pitch).

Figure 14 shows the changes of the contact stiffness and friction coefficient with testing cycle for different contact pressures under high roughness conditions (0.8 mm pitch). Here, the result of normal stiffness under the condition of 900 MPa contact pressure is missing due to sensor failure. It is found that the contact stiffness increases with the contact pressure. It is known that the contact stiffness depends on the contact pressure and increases with the contact pressure [19,43–46]. However, the present result further shows that the higher the contact pressure, the greater the slope of the increase in contact stiffness with increasing number of cycles. Furthermore, the slope of the shear stiffness in the circumferential direction is even larger than that in the radial direction.

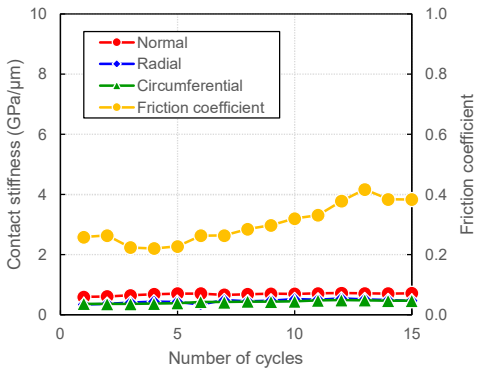

(a) 300 MPa

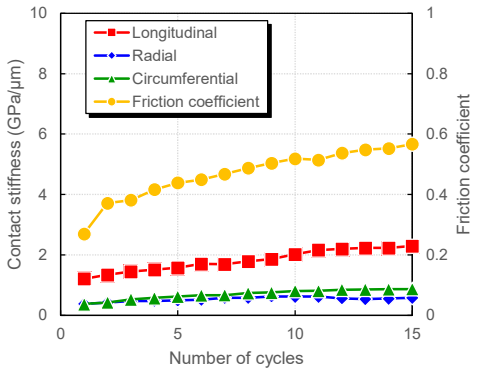

(b) 600 MPa

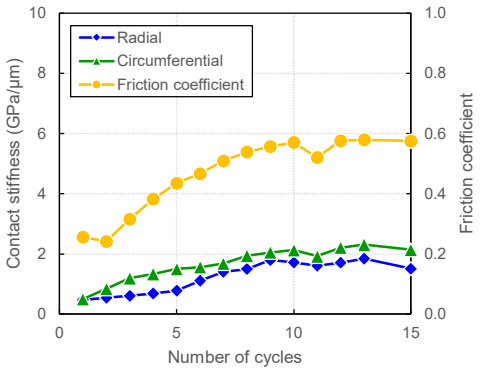

(c) 900 MPa

Fig. 14 Changes of contact stiffness and friction coefficient with test cycles for different contact pressure under high roughness conditions (0.8 mm pitch). (The result of normal stiffness under the condition of 900 MPa contact pressure is missing due to sensor failure.)

3.3 Change in the surface roughness during repetitive cycles

Figure 15 shows the changes of the root mean square roughness and combined roughness with test cycles in different initial roughness.

In the case of low and medium roughness, the roughness of the top and bottom specimens changed in a similar manner. These roughness values increased after the 5th cycle and then increased slowly or remained constant until the 15th cycle. The combined roughness also changed in the same way as the individual roughness of the top and bottom specimens. In the case of high roughness, the roughness of the bottom specimen was higher than that of the top specimen before the test, but as the number of cycles increased, the roughness of the bottom specimen decreased and that of the top specimen increased, finally reaching the same level after the 15th cycle. The combined roughness increased with the number of cycles in the radial direction of 0.4 mm pitch, but the others remained almost constant. The final combined roughness after the 15th cycle was lower in the circumferential direction than in the radial direction for all initial roughness conditions.

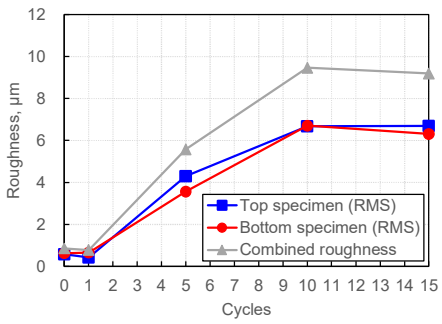

(i) Radial direction

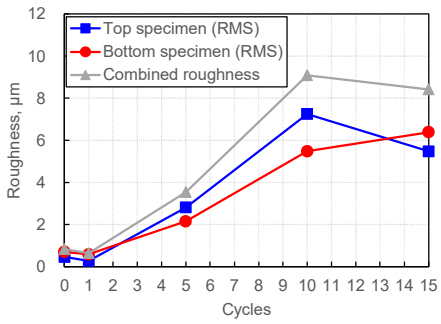

(ii) Circumferential direction

(a) Low roughness

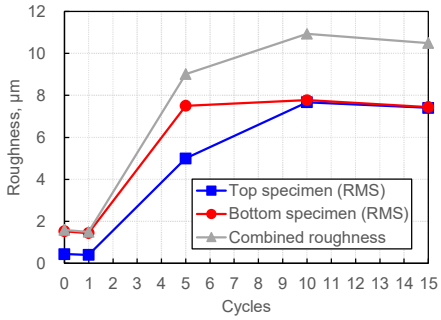

(i) Radial direction

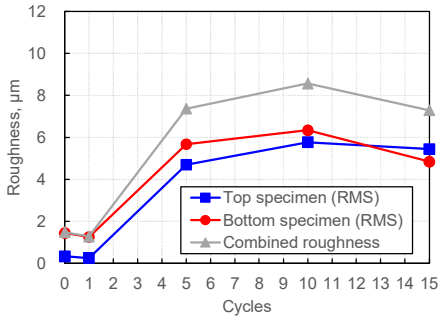

(ii) Circumferential direction

(b) Medium roughness

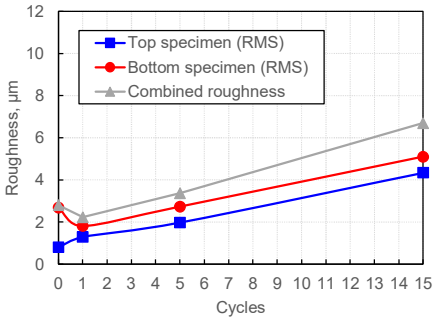

(i) Radial direction

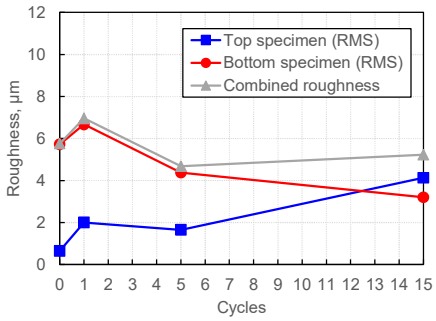

(ii) Circumferential direction

(c) High roughness, 0.4 mm pitch

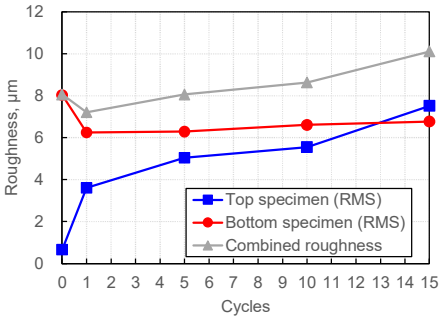

(i) Radial direction

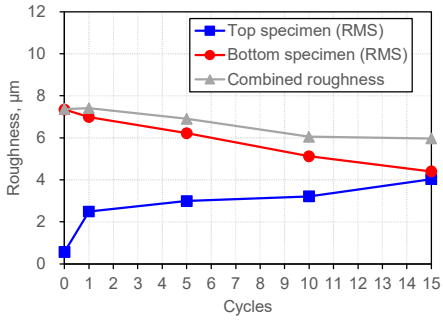

(ii) Circumferential direction

(d) High roughness, 0.8 mm pitch

Fig.15 Changes of the root mean square roughness and combined roughness with test cycles in different initial roughness.

Figure 16 shows the changes of the root mean square roughness and combined roughness with

test cycles for different contact pressure, under high roughness conditions (0.8 mm pitch). For all contact pressure conditions, the roughness values of the bottom and top specimens approached each other as the number of cycles increased, and the higher the contact pressure, the faster these values approached each other. The final combined roughness values in the circumferential direction were lower than those in the radial direction. The Appendix shows the roughness curves of the top and bottom specimens measured with the progress of cycles.

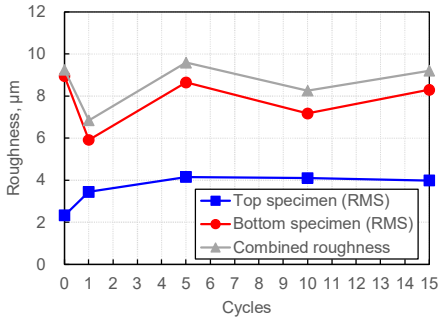

(i) Radial direction

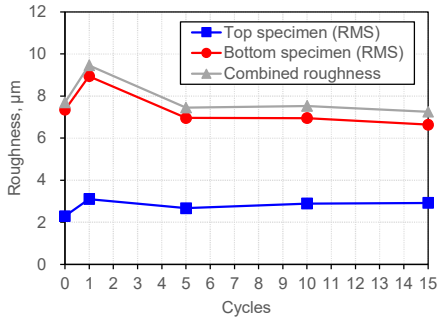

(ii) Circumferential direction

(a) 300 MPa

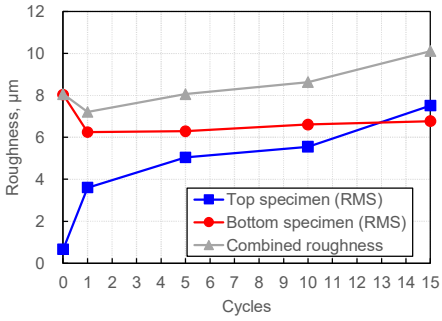

(i) Radial direction

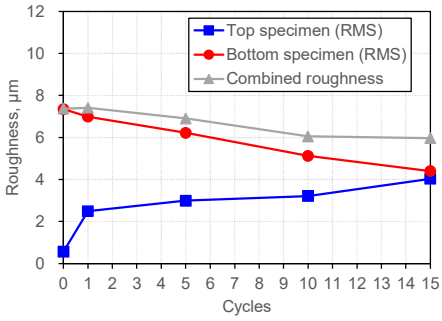

(ii) Circumferential direction

(b) 600 MPa

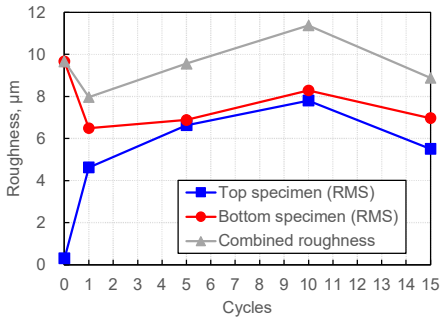

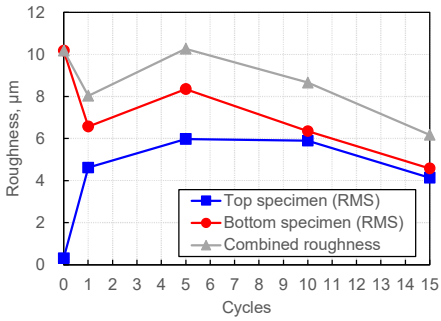

(i) Radial direction (ii) Circumferential direction

(c) 900 MPa

Fig.16 Changes of the root mean square roughness and combined roughness with test cycles in different contact pressure under high roughness conditions (0.8 mm pitch).

4. Discussion

From Fig. 10 and 11, the running-in process can be divided into two main phases; a phase in which the friction coefficient and the contact stiffness are increasing (Phase-I) and decreasing (Phase-II). The distinction between these two phases was clear when the initial roughness was low or medium, but tended to become blurred when the initial roughness was high. This may be due to the elastic-plastic response of the interface influenced by differences in the initial roughness. Based on the whole results, mechanisms for how the surfaces evolve with the repetition of cycles can be proposed. Figure 17 shows a schematic diagram of the running-in process of the interface.

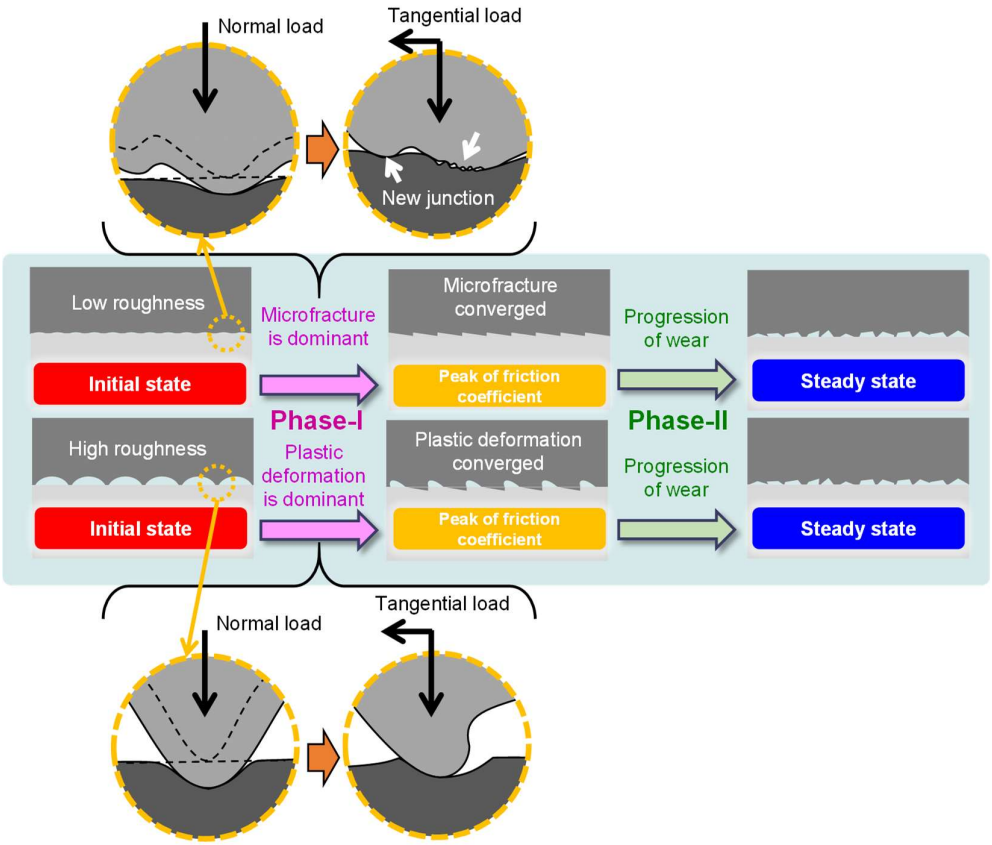

Fig. 17 Schematic mechanism of the difference of the interfacial condition during running-in between low initial roughness and high initial roughness.

In the cases of low and medium roughness, the process was considered as follows;

i. As seen previously for a single cycle [28], asperity junctions form between the surfaces resisting tangential motion. As the Coulomb limit is approached, microscopic fracture occurs, leading to a drop in friction and contact stiffness.
ii. Whilst fracture is microscopic at first, macroslip quickly propogates to the entire interace [37], and un-deformed asperities, previously not in contact, form new adhesion junctions. Stiffness then begins to rise [28], implying an increase in the deformation resistance of the interface, in turn leading to an increase in the coefficient of friction. The fractured junctions also expose fresh metal beneath the original surface, which similarly contribute to an increase in friction coefficient. Hence this process results in the observed overall rise in friction and stiffness over the first cycle.
iii. With repeat cycles, the process continues. Each time the Coulomb limit is reached, interface damage occurs, followed by the formation of new adhesion junctions, as yet more previously undeformed asperities come into contact. Whilst the damaged junctions are weaker and of lower stiffness, the addition of new junctions into the contact leads to a continued net rise in both the interface stiffness and coefficient of friction.
iv. Finally with continued cycles, the surfaces reach a point of conformity, with all asperities having become part of the contact. At this point stiffness and coefficient of friction are maximized.
v. With continued motion and no new asperities available, wear continues at asperity junctions, leading to a drop in stiffness as damage accrues. However, as a fresh metal surface is also exposed continuously, the decrease in the friction coefficient is somewhat gradual, given this removal of material aids junction strength.

i~iii correspond to Phase-I and iv to Phase-II.

In the cases of high roughness, the process was considered as follows;

i. The tips of asperities also conformed, but the penetration of asperities (i.e. each large machined peak) is greater than smoother interface because of the higher local pressure [47].
ii. With the application of tangential load, the asperities plastically deform rather than break bonds owing to the interlocks of the tips by the penetration and the greater heights of asperities. Once Coulomb limit passed and macro-slip occurs, plastic deformation and rounding of surface peaks accelerates [34].
iii. With continued macro-slip, continued deformation and rounding occurs at a gradual rate, and stiffness and friction coefficient rise slowly.

iv. As the plastic deformation of the asperities converges, the micro-slips begin to increase. Throughout this process changes in measured roughness and contact stiffness are marginal, given the wear that occurs is not on the scale of the overall initial surface topography.

i~iii correspond to Phase-I and iv to Phase-II. In the case of 0.4 mm pitch, Phase-II was reached earlier than in the case of 0.8 mm pitch, and partial fracture (micro-slip) wsa considered to have increased after 10th cycle. However, the peak contact stiffness was not as high as for low and medium roughness, indicating that the micro-slip occured partially before the whole asperities were deformed plastically and was expected to spread gradually over the whole contact area.

The contact pressure dependency during the running-in process on contact stiffness and friction coefficient would also support this mechanism. The increase in contact stiffness and friction coefficient was more gradual when the contact pressure was lower (300 MPa). The reason for this is thought to be that the decrease in contact pressure caused more gradual deformation of the surface asperities and more gradual increase in the friction coefficient.

Fantetti *et al.* [31] explained the increase in contact stiffness due to repeated loading and unloading as due to plastic flattening of the asperities, which has been reported by previous researchers [44] and by an author of this paper [33]. Under the conditions of large roughness, it is possible that the similar phenomenon occurred at the beginning of the repetited friction. It is possible that the contact stiffness may have increased as the contacting projections deformed plastically and the overall conformity increased.

In both Figs. 11 and 14, there is a directional dependence of the tangential contact stiffness. The contact stiffness is higher in the circumferential direction (friction direction) than in the radial direction (non-friction direction). This is due to the possibility that the roughness is directional and that when shear load is added, the asperities are more likely to interlock in the circumferential direction than in the radial direction. The fact that this tendency was clearer in the later cycles may indicate that plastic deformation and wear gradually developed, creating a homogenous contact condition over the entire contact surface.

The contact stiffness may also be affected by the tiny wear debris that can be generated at the interface during slip. In the case of the low/medium initial roughness, such wear debris may have been trapped into the gaps formed by the surface asperities, also making the interface more stiff at the peak of the friction coefficient.

Roughness is clearly a strong driver for friction changes in the running in process, and in the measured data, obvious links also exist between the roughness state and the steady state friction. Whilst it would have been desirable to measure the measure roughness after every cycle, and this is something to be considered in the future, further analysis of the pre- and post-test data recorded can help to clarify the trends observed.

Fragmented roughness data is one such analysis approach than can be undertaken to investigate the data further. Figure 18 shows the change of the power spectral density (PSD) obtained from the circumferential roughness curve of the bottom specimens with the increase in the number of cycles in the case of low and high roughness (0.4 mm pitch, 600 MPa) case. It should be noted that these are not the true measured values, but the pseudo-roughness curves obtained by connecting the roughness curves measured five times for 2.4 mm each, and then performing the Fast Fourier Transform. At the PSD before the test, for the high roughness conditions, there are characteristic peaks around the spatial frequencies of 1.25×10^{-3}, which correspond to the fly cutting pitch. For the low roughness conditions, no characteristic peaks were observed. It can be seen that the characteristic peaks of high roughness gradually decrease with the increase in the number of cycles until the 15th cycle. This can be attributed to the gradual plastic deformation of the cutting marks due to normal and tangential pressures.

In the low roughness case, the PSD decreased slightly after the first cycle at a spatial frequency of about 1×10^{-2}, and transformed into a topography with a PSD peak at a spatial frequency of about 2 to 4×10^{-3} from the 5th to the 15th cycle. This may suggest that extreme adhesion and large frictional forces resulted in relatively large scale surface breakdown and caused the decrease the contact stiffness during Phase-II. It should be noted that for the two cases with very different initial roughnesses, a similar surface topography was eventually reached. This trend can be well understood by the change of the roughness curves shown in Appendix.

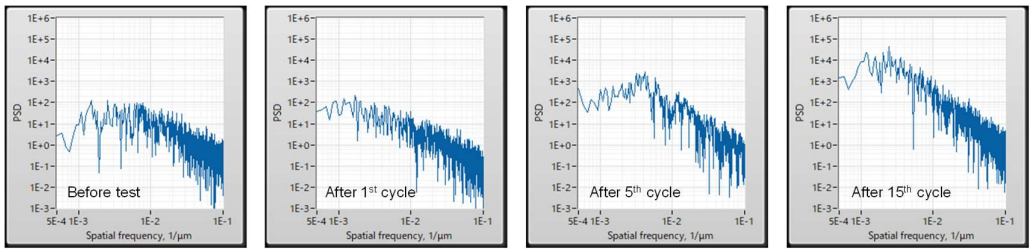

(a) Low roughness

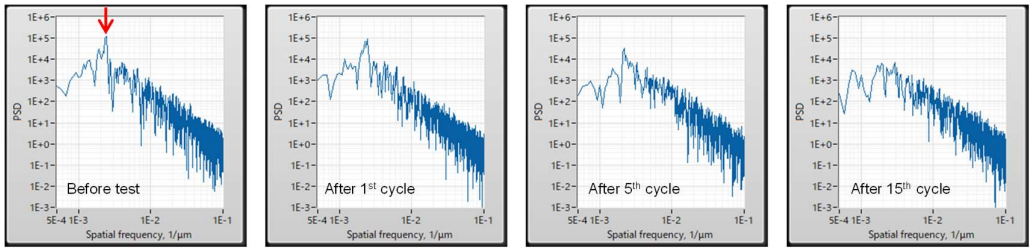

(b) High roughness, 0.4 mm pitch, 600 MPa

Fig. 18 Change of the power spectral density (PSD) obtained from the circumferential roughness curve of the bottom specimens with the increase in the number of cycles. The arrows in (b) refers to the frequencies that can be attributed to the fly cut.

6. Conclusions

Aiming to understand the difference in the running-in behaviour of a wheel-rail interface under different initial roughness conditions and its effect on the friction coefficient, ultrasound reflectometry was applied to the high-pressure torsion test. The high-pressure torsion test cycle was repeated up to 15 times and the change in friction coefficient was monitored and the change in contact stiffness was measured in situ using ultrasound. The following conclusions can be drawn:

(1) The lower the initial roughness, the faster the friction coefficient rose, and the higher the peak friction coefficient value was. These tendencies coincided well with those seen using a twin-disc machine in a previous study [15]. Also, it is found that the rate of increase of friction coefficient in the case of high roughness under 300MPa was lower than 600 MPa and 900 MPa.

(2) In the low roughness condition, the friction coefficient increased with contact stiffness at the beginning of the cyclic test, reached a peak, and then decreased with contact stiffness. While, the change of contact stiffness in the case of high roughness condition linked with that of friction coefficient over the whole test. The change of roughness represented that of contact stiffness well.

(3) A mechanism model during running-in process of the contact interface was proposed as follows; for low initial roughness, the surface fracture was considered to be the dominant factor in increasing the friction coefficient and contact stiffness, whereas for high initial roughness, the plastic deformation of the asperities was considered to be the dominant factor.

These findings will help to understand not only the contact interface after re-profiling of railway wheels, but also the running-in phenomenon of metal-to-metal contact interfaces under high contact pressures.

References

[1] D.I. Fletcher, S.H. Sanusi, The potential for suppressing rail defect growth through tailoring rail thermo-mechanical properties, Wear. 366–367 (2016) 401–406. https://doi.org/10.1016/j.wear.2016.06.022.

[2] J. Ahlström, B. Karlsson, Microstructural evaluation and interpretation of the mechanically and thermally affected zone under railway wheel flats, Wear. 232 (1999) 1–14. https://doi.org/10.1016/S0043-1648(99)00166-0.

[3] S. Fukagai, T. Toyama, T. Tanaka, M. Kuzuta, H. Doi, Visualization of wheel-rail contact area of running vehicle using film sensor, Proc. Inst. Mech. Eng. Part F J. Rail Rapid Transit. (2021).

https://doi.org/10.1177/09544097211041841.

[4] R. Lewis, R.S. Dwyer-Joyce, U. Olofsson, J. Pombo, J. Ambrósio, M. Pereira, C. Ariaudo, N. Kuka, Mapping railway wheel material wear mechanisms and transitions, Proc. Inst. Mech. Eng. Part F J. Rail Rapid Transit. 224 (2010) 125–137. https://doi.org/10.1243/09544097JRRT328.

[5] U. Olofsson, T. Telliskivi, Wear, plastic deformation and friction of two rail steels - A full-scale test and a laboratory study, Wear. 254 (2003) 80–93. https://doi.org/10.1016/S0043-1648(02)00291-0.

[6] S. Kumar, G. Yu, A.C. Witte, Wheel-rail resistance and energy consumption analysis of cars on tangent track with different lubrication strategies, Proc. IEEE/ASME Jt. Railr. Conf. (1995) 129–136. https://doi.org/10.1109/rrcon.1995.395159.

[7] D.T. Eadie, M. Santoro, J. Kalousek, Railway noise and the effect of top of rail liquid friction modifiers: Changes in sound and vibration spectral distributions in curves, Wear. 258 (2005) 1148–1155. https://doi.org/10.1016/j.wear.2004.03.061.

[8] S. Fukagai, T. Ban, M. Ogata, M. Ishida, A. Namura, Development of wheel/rail Friction Moderating System (FRIMOS), Q. Rep. RTRI (Railw. Tech. Res. Institute). 49 (2008). https://doi.org/10.2219/rtriqr.49.26.

[9] W.C. Shust, J.A. Elkins, Wheel forces during flange climb part I - track loading vehicle tests, in: Railr. Conf. 1997., Proc. 1997 IEEE/ASME Joint., 1997: pp. 137–147.

[10] H. Ishida, T. Miyamoto, E. Maebashi, H. Doi, K. Iida, A. Furukawa, Safety assessment for flange climb derailment of trains running at low speeds on sharp curves, Q. Rep. RTRI. 47 (2006) 65–71. https://doi.org/10.2219/rtriqr.47.65.

[11] A. Matsumoto, Y. Sato, H. Ohno, M. Tomeoka, K. Matsumoto, J. Kurihara, T. Ogino, M. Tanimoto, Y. Kishimoto, Y. Sato, T. Nakai, A new measuring method of wheel-rail contact forces and related considerations, Wear. 265 (2008) 1518–1525. https://doi.org/10.1016/j.wear.2008.02.031.

[12] S. Greene, G. Cook, N.P. Ford, R.L. Freeland, F.M. Gilliam, J. a Hough, R.H. Irwin, G.G. Bridge, D. a Lee, Flange Climb Derailment Criteria and Wheel/Rail Profile Management and Maintenance Guidelines for Transit Operations, TCRP Rep. 71 Track-Related Res. 5 (2005) 147.

[13] R.A.I. Branch, Rail Accident Report, Locomotive derailment at Ordsall Lane Junction, Salford, 23 January 2013, 2014. https://assets.publishing.service.gov.uk/media/547c8fbb40f0b60241000159/R072014_140331_Ordsall_Lane_Junction.pdf.

[14] R.A.I. Branch, Safety digest, Locomotive derailment at Doncaster, 21 December 2018, 2019.

[15] S. Fukagai, L. Ma, R. Lewis, Tribological aspects to optimize traction coefficient during running-in period using surface texture, Wear. 424–425 (2019) 223–232. https://doi.org/10.1016/j.wear.2019.02.023.

[16] H.M. Cao, X. Zhou, X.Y. Li, K. Lu, Friction mechanism in the running-in stage of copper: From

plastic deformation to delamination and oxidation, Tribol. Int. 115 (2017) 3–7. https://doi.org/10.1016/j.triboint.2017.05.027.

[17] J. Shimizu, T. Nakayama, K. Watanabe, T. Yamamoto, T. Onuki, H. Ojima, L. Zhou, Friction characteristics of mechanically microtextured metal surface in dry sliding, Tribol. Int. 149 (2020) 105634. https://doi.org/10.1016/j.triboint.2019.02.042.

[18] M. Pau, Estimation of real contact area in a wheel-rail system by means of ultrasonic waves, Tribol. Int. 36 (2003) 687–690. https://doi.org/10.1016/S0301-679X(03)00014-8.

[19] M.B. Marshall, R. Lewis, R.S. Dwyer-Joyce, U. Olofsson, S. Björklund, Experimental Characterization of Wheel-Rail Contact Patch Evolution, J. Tribol. 128 (2006) 493–503. https://doi.org/10.1115/1.2197523.

[20] R.S. Dwyer-Joyce, C. Yao, J. Zhang, R. Lewis, B.W. Drinkwater, Feasibility Study for Real Time Measurement of Wheel-Rail Contact Using an Ultrasonic Array, J. Tribol. 131 (2009) 041401. https://doi.org/10.1115/1.3176992.

[21] M. Pau, B. Leban, Ultrasonic assessment of wheel-rail contact evolution exposed to artificially induced wear, Proc. Inst. Mech. Eng. Part F J. Rail Rapid Transit. 223 (2009) 353–364. https://doi.org/10.1243/09544097JRRT241.

[22] R.S. Dwyer-Joyce, C. Yao, R. Lewis, H. Brunskill, An ultrasonic sensor for monitoring wheel flange/rail gauge corner contact, Proc. Inst. Mech. Eng. Part F J. Rail Rapid Transit. 227 (2013) 188–195. https://doi.org/10.1177/0954409712460986.

[23] H. Brunskill, A. Hunter, L. Zhou, R. Dwyer Joyce, R. Lewis, An evaluation of ultrasonic arrays for the static and dynamic measurement of wheel–rail contact pressure and area, Proc. Inst. Mech. Eng. Part J J. Eng. Tribol. 234 (2020) 1580–1593. https://doi.org/10.1177/1350650120919889.

[24] L. Zhou, H.P. Brunskill, R. Lewis, M.B. Marshall, R.S. Dwyer-Joyce, Dynamic characterisation of the wheel/rail contact using ultrasonic reflectometry, Civil-Comp Proc. 104 (2014) 1–13.

[25] L. Zhou, H.P. Brunskill, R. Lewis, Real-time non-invasive measurement and monitoring of wheel–rail contact using ultrasonic reflectometry, Struct. Heal. Monit. 0 (n.d.) 1475921719829882. https://doi.org/10.1177/1475921719829882.

[26] K. Kendall, D. Tabor, An Ultrasonic Study of the Area of Contact between Stationary and Sliding Surfaces, Proc. R. Soc. A Math. Phys. Eng. Sci. 323 (1971) 321–340. https://doi.org/10.1098/rspa.1971.0108.

[27] H.G. Tattersall, The ultrasonic pulse-echo technique as applied to adhesion testing, J. Phys. D. Appl. Phys. 6 (1973) 819–832.

[28] A. Rovira, A. Roda, M.B. Marshall, H. Brunskill, R. Lewis, Experimental and numerical modelling of wheel-rail contact and wear, Wear. 271 (2011) 911–924. https://doi.org/10.1016/j.wear.2011.03.024.

[29] M. Pau, B. Leban, M. Guagliano, Propagation of Sub-surface Cracks in Railway Wheels for Wear-

induced Conformal Contacts, J. Mech. Syst. Transp. Logist. 3 (2010) 226–235. https://doi.org/10.1299/jmtl.3.226.

[30] L. Pesaresi, A. Fantetti, F. Cegla, L. Salles, C.W. Schwingshackl, On the Use of Ultrasound Waves to Monitor the Local Dynamics of Friction Joints, Exp. Mech. (2019). https://doi.org/10.1007/s11340-019-00550-y.

[31] A. Fantetti, S. Mariani, L. Pesaresi, D. Nowell, F. Cegla, C. Schwingshackl, Ultrasonic monitoring of friction contacts during shear vibration cycles, Mech. Syst. Signal Process. 161 (2021). https://doi.org/10.1016/j.ymssp.2021.107966.

[32] S. Fukagai, H.P. Brunskill, A.K. Hunter, R.S. Dwyer-Joyce, R. Lewis, Transitions in rolling-sliding wheel/rail contact condition during running-in, Tribol. Int. 149 (2020) 105679. https://doi.org/10.1016/j.triboint.2019.03.037.

[33] S. Fukagai, T. Ban, K. Makino, M. Kuzuta H. Chen, H. Brunskill, R.S. Dwyer-Joyce, Using Active Ultrasonics to Measure Wheel-Rail Contact During a Running-in Period, Int. J. Railw. Technol. 7 (2018) 1–20. https://doi.org/10.4203/ijrt.7.3.1.

[34] S. Fukagai, M. Watson, H.P. Brunskill, A.K. Hunter, M.B. Marshall, R. Lewis, In situ evaluation of contact stiffness in a slip interface with different roughness conditions using ultrasound reflectometry, Proc. R. Soc. A. 477 (2021) 20210442.

[35] M. Evans, W.A. Skipper, L. Buckley-Johnstone, A. Meierhofer, K. Six, R. Lewis, The development of a high pressure torsion test methodology for simulating wheel/rail contacts, Tribol. Int. 156 (2021) 106842. https://doi.org/10.1016/j.triboint.2020.106842.

[36] B.W. Drinkwater, R.S. Dwyer-Joyce, P. Cawley, A study of the interaction between ultrasound and a partially contacting solid—solid interface, Proc. R. Soc. London. Ser. A Math. Phys. Eng. Sci. 452 (1996) 2613–2628. https://doi.org/10.1098/rspa.1996.0139.

[37] R.S. Dwyer-Joyce, The application of ultrasonic NDT techniques in tribology, Proc. Inst. Mech. Eng. Part J J. Eng. Tribol. 219 (2005) 347–366. https://doi.org/10.1243/135065005X9763.

[38] R.S. Dwyer-Joyce, M. Gonzalez-Valadez, Ultrasonic Determination of Normal and Shear Interface Stiffness and the Effect of Poisson' s Ratio., Transient Process. Tribol. (2004) 143–149.

[39] M. Gonzalez-Valadez, A. Baltazar, R.S. Dwyer-Joyce, Study of interfacial stiffness ratio of a rough surface in contact using a spring model, Wear. 268 (2010) 373–379. https://doi.org/10.1016/j.wear.2009.08.022.

[40] J.J. O'Connor, K.L. Johnson, The role of surface asperities in transmitting tangential forces between metals, Wear. 6 (1963) 118–139. https://doi.org/10.1016/0043-1648(63)90125-X.

[41] J. Królikowski, J. Szczepek, Assessment of tangential and normal stiffness of contact between rough surfaces using ultrasonic method, Wear. 160 (1993) 253–258. https://doi.org/10.1016/0043-1648(93)90428-O.

[42] S. Medina, D. Nowell, D. Dini, Analytical and numerical models for tangential stiffness of rough

elastic contacts, Tribol. Lett. 49 (2013) 103–115. https://doi.org/10.1007/s11249-012-0049-y.

[43] B. Drinkwater, R. Dwyer-Joyce, P. Cawley, A Study of the Transmission of Ultrasound Across Real Rough Solid-Solid Interfaces, in: D.O. Thompson, D.E. Chimenti (Eds.), Rev. Prog. Quant. Nondestruct. Eval. Vol. 14, Springer US, Boston, MA, 1995: pp. 1829–1836. https://doi.org/10.1007/978-1-4615-1987-4_234.

[44] R.S. Dwyer-Joyce, B.W. Drinkwater, A.M. Quinn, The Use of Ultrasound in the Investigation of Rough Surface Interfaces, J. Tribol. 123 (2001) 8. https://doi.org/10.1115/1.1330740.

[45] J.Y. Kim, A. Baltazar, S.I. Rokhlin, Ultrasonic assessment of rough surface contact between solids from elastoplastic loading-unloading hysteresis cycle, J. Mech. Phys. Solids. 52 (2004) 1911–1934. https://doi.org/10.1016/j.jmps.2004.01.006.

[46] S. Biwa, S. Hiraiwa, E. Matsumoto, Stiffness evaluation of contacting surfaces by bulk and interface waves, Ultrasonics. 47 (2007) 123–129. https://doi.org/10.1016/J.ULTRAS.2007.08.005.

[47] N. Nagase, S. Shido, I. Yarita, The effect of lubricant on microwear of dull rolls in temper rolling by 4 hi rolling mill, ISIJ Int. 49 (2009) 874–880. https://doi.org/10.2355/isijinternational.49.874.

Appendix

Table A.1 Change of roughness curves of the top and bottom specimens with the progress of the cycles in the case of low roughness when the contact stress is 600 MPa.

	Top/Bottom	Circumferential direction	Radial direction
Initial	Top	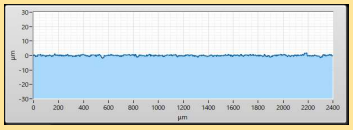	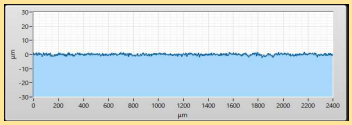
	Bottom	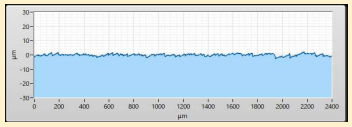	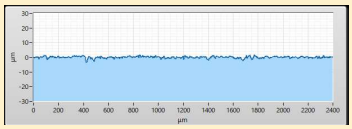
After 1st cycle	Top	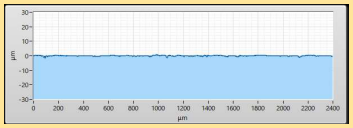	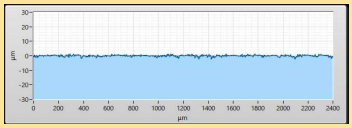
	Bottom	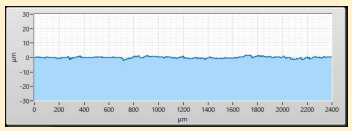	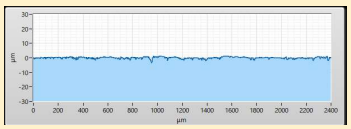
After 5th cycle	Top	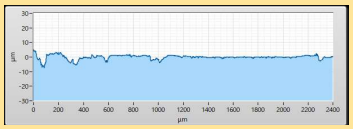	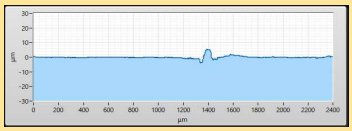
	Bottom	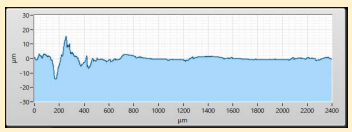	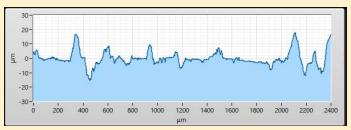
After 10th cycle	Top	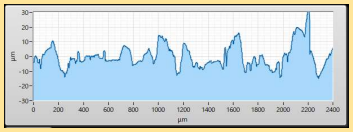	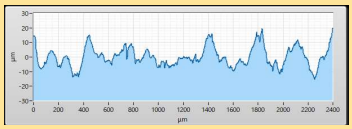
	Bottom	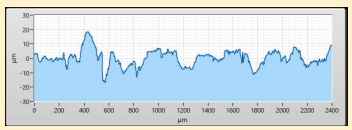	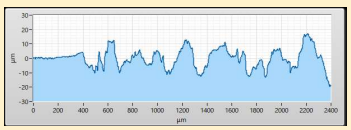
After 15th cycle	Top	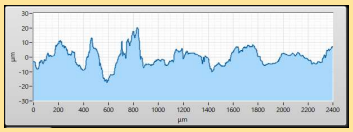	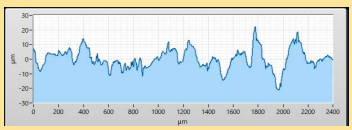
	Bottom	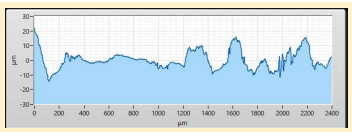	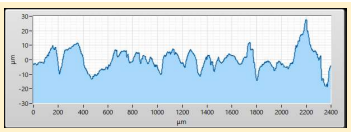

Table A.2 Change of roughness curves of the top and bottom specimens with the progress of the cycles in the case of medium roughness when the contact stress is 600 MPa.

	Top/Bottom	Circumferential direction	Radial direction
Initial	Top	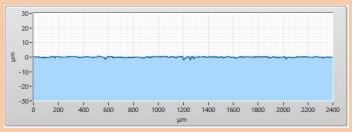	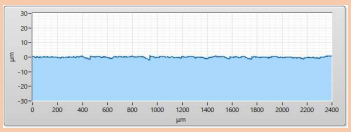
	Bottom	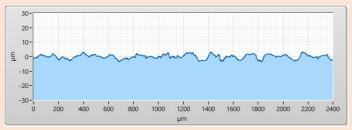	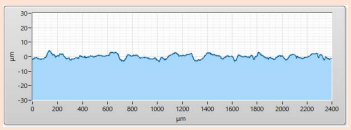
After 1st cycle	Top	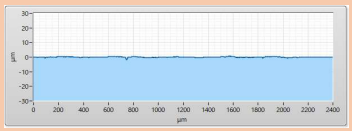	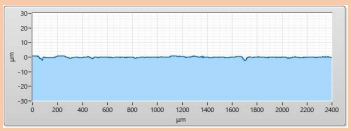
	Bottom	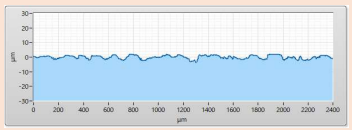	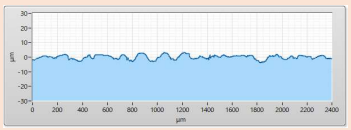
After 5th cycle	Top	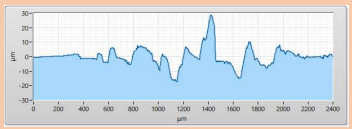	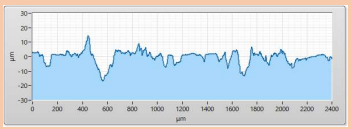
	Bottom	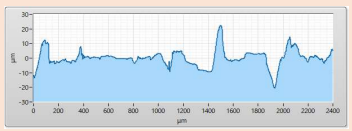	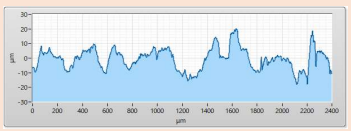
After 10th cycle	Top	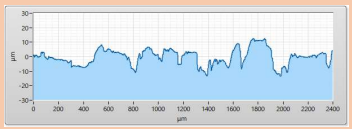	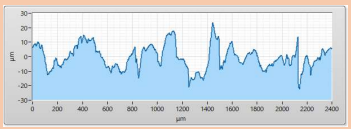
	Bottom	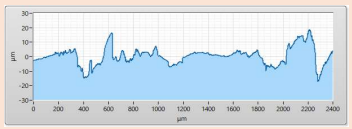	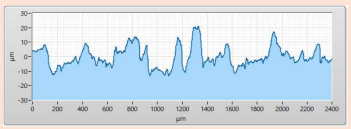
After 15th cycle	Top	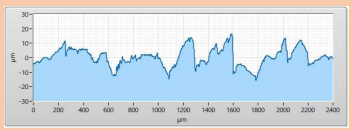	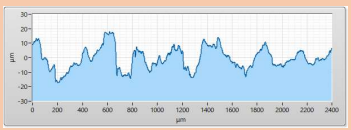
	Bottom	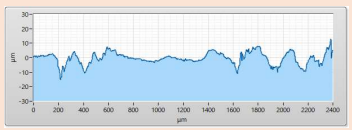	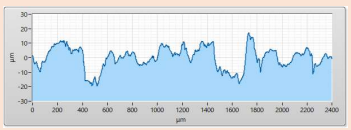

Table A.3 Change of roughness curves of the top and bottom specimens with the progress of the cycles in the case of high roughness (0.4 mm pitch) when the contact stress is 600 MPa.

	Top/Bottom	Circumferential direction	Radial direction
Initial	Top	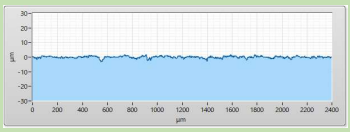	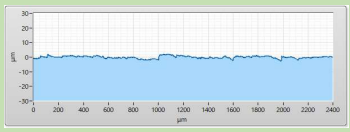
	Bottom		
After 1st cycle	Top	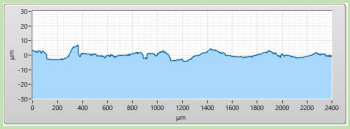	
	Bottom		
After 5th cycle	Top		
	Bottom		
After 15th cycle	Top	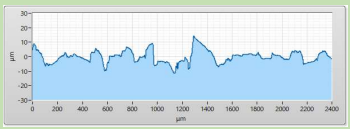	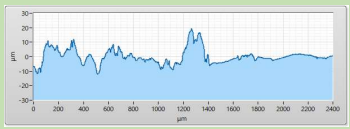
	Bottom	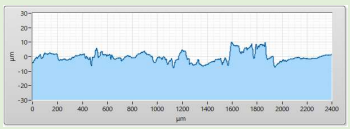	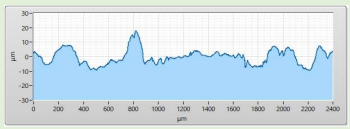

Table A.4 Change of roughness curves of the top and bottom specimens with the progress of the cycles in the case of high roughness (0.8 mm pitch) when the contact stress is 600 MPa.

	Top/Bottom	Circumferential direction	Radial direction
Initial	Top	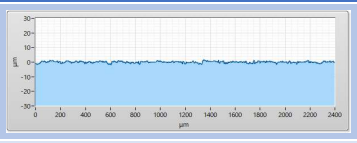	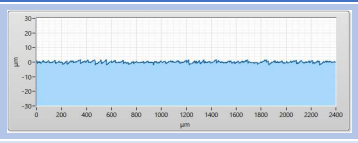
	Bottom	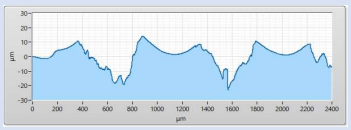	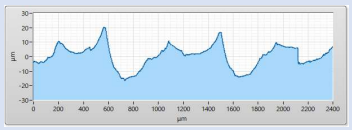
After 1st cycle	Top	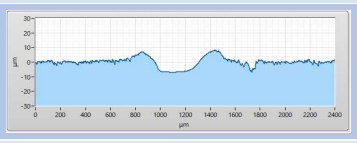	
	Bottom	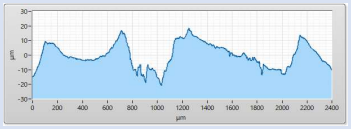	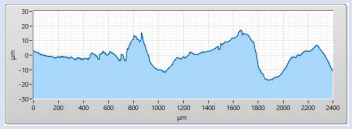
After 5th cycle	Top	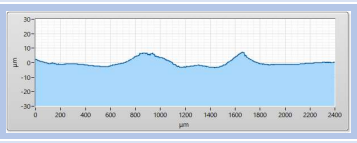	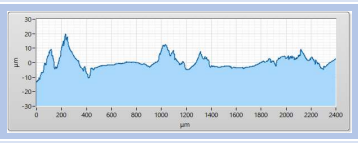
	Bottom		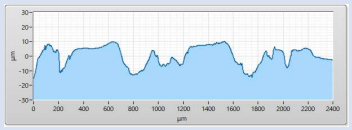
After 10th cycle	Top		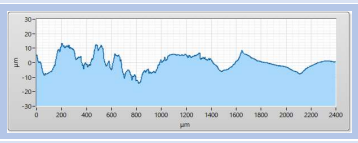
	Bottom	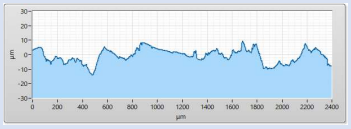	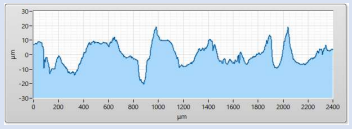
After 15th cycle	Top		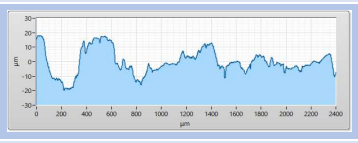
	Bottom	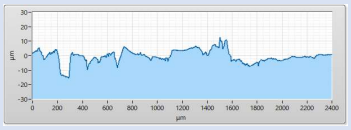	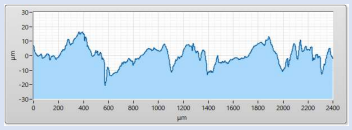

Table A.5 Change of roughness curves of the top and bottom specimens with the progress of the cycles in the case of high roughness (0.8 mm pitch) when the contact stress is 300 MPa.

	Top/Bottom	Circumferential direction	Radial direction
Initial	Top	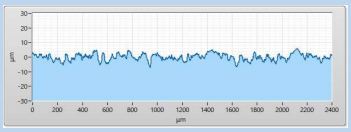	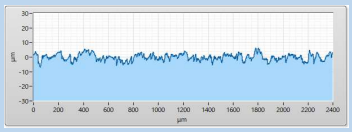
	Bottom	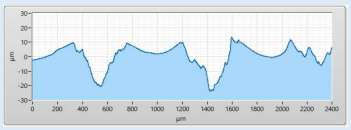	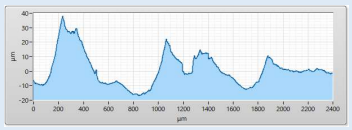
After 1st cycle	Top	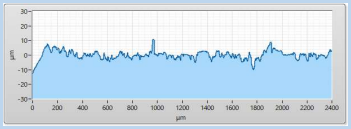	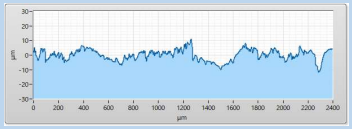
	Bottom	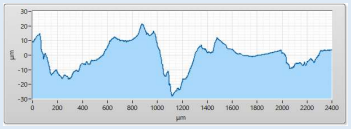	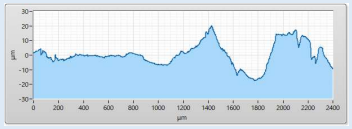
After 5th cycle	Top	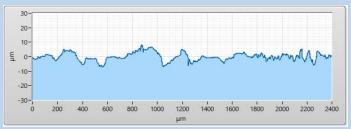	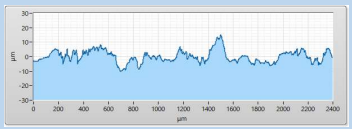
	Bottom	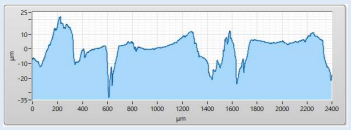	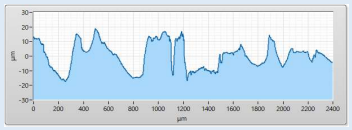
After 10th cycle	Top	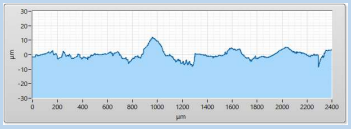	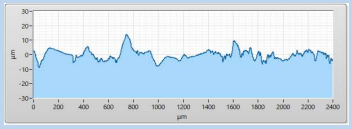
	Bottom	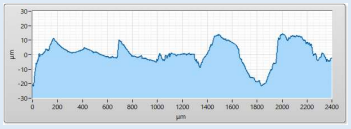	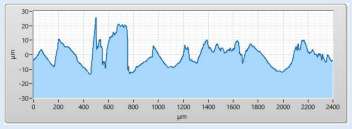
After 15th cycle	Top	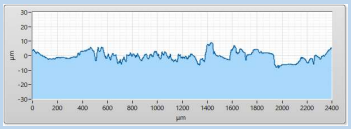	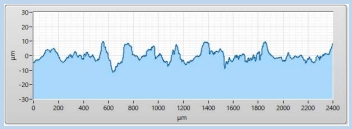
	Bottom	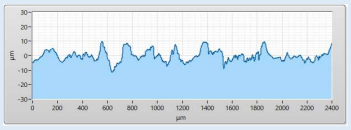	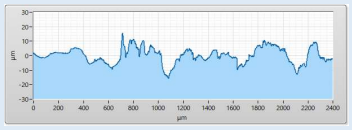

Table A.6 Change of roughness curves of the top and bottom specimens with the progress of the cycles in the case of high roughness (0.8 mm pitch) when the contact stress is 900 MPa.

	Top/Bottom	Circumferential direction	Radial direction
Initial	Top	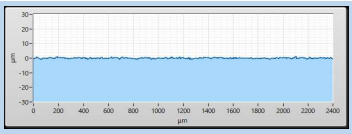	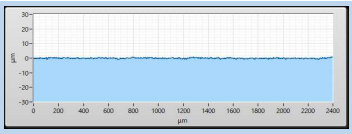
	Bottom	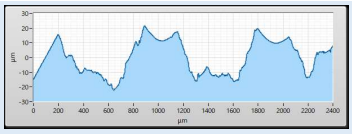	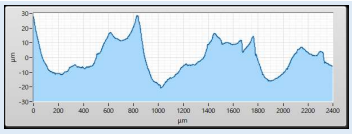
After 1st cycle	Top	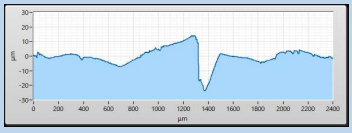	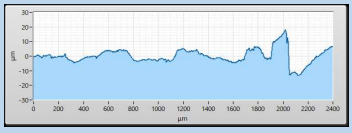
	Bottom	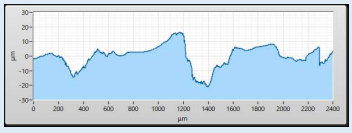	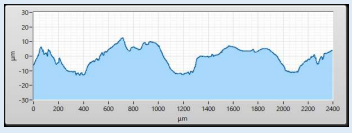
After 5th cycle	Top	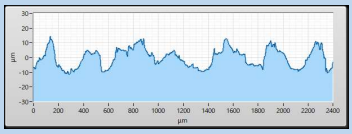	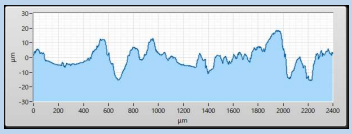
	Bottom	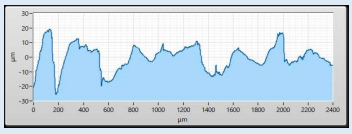	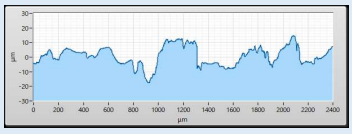
After 10th cycle	Top	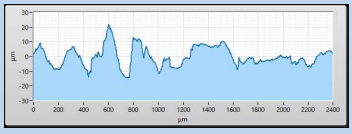	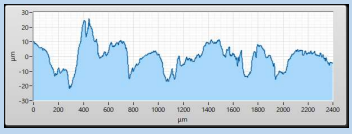
	Bottom	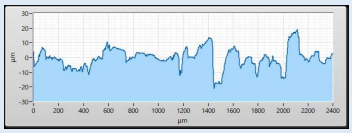	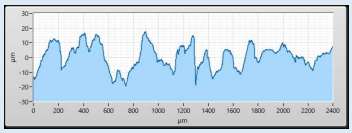
After 15th cycle	Top	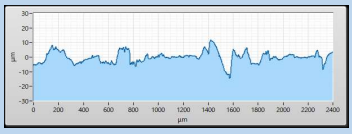	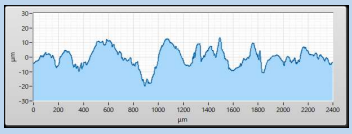
	Bottom